Journal of Alloys and Compounds 828 (2020) 154409

Contents lists available at ScienceDirect

Journal of Alloys and Compounds

journal homepage: http://www.elsevier.com/locate/jalcom

Influence of ferrite to silica ratio and thermal treatment on porosity, surface, microstructure and magnetic properties of $Zn_{0.5}Ni_{0.5}Fe_2O_4/SiO_2$ nanocomposites

Thomas Dippong [a], Oana Cadar [b], Iosif Grigore Deac [c], Mihaela Lazar [d], Gheorghe Borodi [d], Erika Andrea Levei [b, *]

[a] Technical University of Cluj-Napoca, North University Center of Baia Mare, Department of Chemistry and Biology, 76 Victoriei Street, 430122, Baia Mare, Romania
[b] INCDO-INOE 2000, Research Institute for Analytical Instrumentation, 67 Donath Street, 400293, Cluj-Napoca, Romania
[c] Babes-Bolyai University, Faculty of Physics, 1 Kogalniceanu Street, 400084, Cluj-Napoca, Romania
[d] National Institute for Research and Development of Isotopic and Molecular Technologies, 65-103 Donath Street, 400293, Cluj-Napoca, Romania

ARTICLE INFO

Article history:
Received 4 December 2019
Received in revised form
15 February 2020
Accepted 16 February 2020
Available online 18 February 2020

Keywords:
Nanocomposites
Zinc-nickel ferrite
Magnetic properties
Specific surface area
Porosity
Crystallinity

ABSTRACT

The evolution of structural and magnetic properties of $Zn_{0.5}Ni_{0.5}Fe_2O_4/SiO_2$ nanocomposites with the ferrite content embedded in the SiO_2 matrix and the annealing temperature was investigated. The results showed the increase of crystallite size (2.7−57.4 nm), saturation magnetization (0.36−82.4 emu/g), remanence magnetization (0.06−15.4 emu/g) and the decrease of specific pore volume (0.183 −0.010 cm^3/g) and specific surface area ($\leq$0.5−247 m^2/g) with the increase of $Zn_{0.5}Ni_{0.5}Fe_2O_4$ content embedded in the SiO_2 matrix and the annealing temperature. The SiO_2 matrix exhibits diamagnetic behavior with a small ferromagnetic fraction, $Zn_{0.5}Ni_{0.5}Fe_2O_4$ embedded in SiO_2 matrix presents superparamagnetic-like behavior, while bulk $Zn_{0.5}Ni_{0.5}Fe_2O_4$ a high-quality ferromagnetic type behavior.

1. Introduction

Crystalline spinel ferrites with the general formula MFe_2O_4, where M is a divalent metal ion such as Fe^{2+}, Mg^{2+}, Ni^{2+}, Co^{2+}, Mn^{2+} are ferrimagnetic materials with special structure and electrical, magnetic and dielectric properties [1]. The high surface area-to-volume ratio, surface chemistry and morphology, along with the high density of imperfections in the nanocrystalline structure make ferrites attractive materials for various technological applications [2]. Generally, the ferrite properties are very sensitive to chemical composition, microstructure, cation distribution, preparation conditions, applied thermal treatment, dopant type and amount [1,3]. The structural and microstructural characteristics of ferrites (particle size and cation distribution among tetrahedral and octahedral sites of the spinel lattice) are strongly dependent on the preparation method [4]. Also, the spinel ferrites composition influences the structural phase heterogeneity and physical properties [2]. The doping of spinel ferrites with various transitional metals improves their electrical and magnetic properties, while their embedding in SiO_2 matrix allows a better control of the particle size by preventing their agglomeration [1]. Furthermore, combined with thermal treatment at high temperatures, it favors the formation of nanoscale single-phase spinel structures with enhanced magnetic properties [5].

A considerable number of synthesis methods for spinel ferrites, such as sol-gel method, ball-milling, co-precipitation, hydrothermal precipitation, spray pyrolysis, citrate precursor, auto-combustion, solid state reaction, microwave assisted hydrothermal or solid state reaction, mechanical alloying, micro-emulsion, sonochemical, reactive or high energy ball milling, pulsed wire discharge and reverse micelle were reported in the literature [6−11]. The main disadvantages of these synthesis methods are the complexity, high reaction temperature, long reaction time, use of toxic chemicals and the difficulty to control the process due to the

* Corresponding author.
E-mail address: erika.levei@icia.ro (E.A. Levei).

https://doi.org/10.1016/j.jallcom.2020.154409
0925-8388/

formation of unwanted phases [2,7,9,10,13]. During the ball-milling process, the powdered materials suffer collisions with the grinding media, leading to a homogeneous mixture and allowing a good control over the particles size [2,8,10,11]. The plasma arc discharge technique is also a very simple, inexpensive and flexible route for preparation of nanocrystalline materials [4]. The sol-gel method allows outstanding control over the composition, size and homogeneity of the nanoparticles [2,12].

Ni–Zn soft magnetic ferrite is one of the most important ferromagnetic ceramic materials due to the low coercivity (H_c) and eddy current loses, but high electrical permeability, resistivity, mechanical hardness, surface area, Curie temperature and chemical stability. These properties allow their use for the development of new applications or devices in medicine, electronics, ceramics, sensors, catalysis, water purification or refrigeration [1,4,13,14].

Our previous studies revealed the structural, morphological and magnetic properties of $Co_xFe_{3-x}O_4$ [15], $Ni_xCo_{1-x}Fe_2O_4$ [16] and $Zn_xCo_{1-x}Fe_2O_4$ [17] embedded in SiO_2 matrix, synthesized by sol-gel method followed by annealing at different temperatures. This paper presents the effect of $Zn_{0.5}Ni_{0.5}Fe_2O_4$ content embedded in SiO_2 matrix and of annealing temperature on the structure (crystallite size, crystallinity), surface (specific surface area and porosity), morphology (particle shape and size) and magnetic properties (saturation and remanent magnetization, coercivity) of $Ni_{0.5}Zn_{0.5}Fe_2O_4/SiO_2$ nanocomposites (NCs).

2. Materials and methods

Analytical grade chemicals were used without further purification. The sol-gel method was used for the synthesis of $\delta Zn_{0.5}Ni_{0.5}Fe_2O_4/(100-\delta)SiO_2$ (δ = 10, 25, 50, 75, 100%) NCs. Zinc nitrate ($Zn(NO_3)_2$ $6H_2O$), nickel nitrate ($Ni(NO_3)_2$ $6H_2O$) and iron nitrate ($Fe(NO_3)_3$ $9H_2O$) were dissolved in 1,4-butanediol in a molar ratio of 0.5:0.5:2:8. An ethanolic solution of tetraethyl orthosilicate (TEOS) was added drop-wise to this mixture, under continuous stirring, using a NO_3^-:TEOS molar ratio of 0:2 (δ = 0%), 0.5:1.5 (δ = 25%), 1:1 (δ = 50%), 1.5:0.5 (δ = 75%) and 2:0 (δ = 100%). The resulted sols were acidulated to pH = 2 using nitric acid and exposed to open air for slow gelation. The gels were grinded and dried at 40 °C for 5 h, heated in an oven at 200 °C for 5 h, and then annealed at 400, 700 and 1000 °C for 5 h.

The phase transformations during thermal decomposition were investigated by thermogravimetry (TG) and differential thermal analysis (DTA) using an Q600 SDT (TA Instruments) simultaneous thermal analyzer, in air up to 1000 °C, at 10 °C/min and alumina standards. The formation and decomposition of functional groups was studied by Spectrum BX II (Perkin Elmer) Fourier-transform infrared spectrometer (FT-IR) on KBr pellets containing 1% (w/w) sample. The X-ray diffraction patterns were recorded at room temperature, using a D8 Advance (Bruker) diffractometer, operating at 40 kV and 40 mA with CuK_α radiation (λ = 1.54060 Å). The nanoparticles shape and clustering were studied on samples deposited from suspension onto carbon film coated copper grids using a HD-2700 (Hitachi) scanning transmission electron microscope (TEM) equipped with digital image recording system and photographic film image with high resolution scanner. Specific surface area (SSA) was obtained using the BET model from N_2 adsorption-desorption isotherms recorded at −196 °C by a Sorptomatic 1990 (Thermo Fisher Scientific) instrument. The pore size distribution was calculated from the desorption branch of the isotherm using the Dollimore Heal model. Before determination, the samples were degassed for 4 h at 150 °C and 2 Pa pressure, in order to remove the physisorbed impurities from the surface. No pressure variation was observed during 1 h at the end of the degassing process. The magnetic measurements were performed using a cryogen-free vibrating-sample magnetometer (Cryogenic Limited). The hysteresis loops were recorded in magnetic fields between −2 and 2 T, at room temperature, while the magnetization versus magnetic field measurements were performed to find the saturation magnetization (M_S) up to 5 T, on samples embedded in epoxy resin to prevent the nanoparticle movement.

3. Results and discussion

3.1. Thermal analysis

The TG-DTA diagrams of gels heated at 40 °C are shown in Fig. 1. In case of gel δ = 0%, that does not contain nitrates, a weak endothermic effect at 59 °C attributed to the loss of structural water from TEOS and an exothermic effect at 299 °C attributed to the decomposition of the diol are observed [18]. In case of gels δ = 25, 50, 75%, the total mass loss increases from 47 to 65% with the increase of the ferrite content. The endothermic peak at 70–89 °C is attributed to crystallization water loss from the nitrates and SiO_2 matrix. The exothermic effects attributed to the formation and decomposition of metal succinates slightly shifts from 145 to 178 °C and from 270 to 295 °C, with the decrease of SiO_2 contents. The splitting tendency of the exothermic peak in the range of 280–300 °C for gel δ = 75%, could be explained by the decomposition of metal succinates into ferrites at close temperatures [19]. The DTA diagram of gel δ = 100%, shows five thermal effects and a total mass loss of 68%, attributed to crystallization water loss from nitrates (81 °C), formation of metal-succinate precursors (140 °C, 176 °C) and precursors decomposition with ferrite formation (261 °C, 298 °C). The presence of SiO_2 matrix that undergoes various transformations during the thermal process makes more difficult the delimitation of the processes attributed to the formation and decomposition of succinates.

3.2. FT-IR analysis

The FT-IR spectra of samples heated at 40 and 200 °C are shown in Fig. 2. Except for sample δ = 0 that does not contain nitrates, the spectra of samples dried at 40 °C shows the presence of a band at 1387 cm^{-1}, characteristic to nitrates. This band does not appear in the spectra of samples heated at 200 °C indicating the full decomposition of nitrates up to this temperature [15,18]. In all samples heated both at 40 and 200 °C, except for bulk ferrite (δ = 100%), the presence of SiO_2 matrix is indicated by the specific bands for vibration of Si–O bond (435–454 cm^{-1}) and of Si–O–Si structures (577–580, 792–829, 1046-1068 cm^{-1}) [15,20,21]. The bands around 3400-3200 cm^{-1} are attributed to O–H stretching and intermolecular hydrogen bonds in 1,4-butanediol (40 °C) and succinate precursor (200 °C) [6,18]. The band at 1680-1667 cm^{-1} in samples heated at 40 °C is attributed to vibrations of O–H from 1,4-butanediol and adsorbed molecular water, while the bands at 2956-2943 and 2887-2874 cm^{-1} to the asymmetric and symmetric stretching vibration of the C–H bond in diols [18].

In samples with δ = 25–100% heated to 200 °C, the presence of the band at 1677-1611 cm^{-1} attributed to vibration of C=O in COO^- groups confirms formation of a chelated complex by the coordination of carboxylate groups by metal ions [16].

Fig. 3 shows the FT-IR spectra and XRD patterns of NCs annealed at 400, 700 and 1000 °C. In the FT-IR spectra of δ = 25, 50 and 75% NCs, the presence of the SiO_2 matrix is confirmed by the symmetric and asymmetric vibrations of SiO_4 tetrahedron at 804-792 cm^{-1}, the Si–O–Si stretching vibrations at 1108-1064 cm^{-1} and the Si–O bond vibration at 475-447 cm^{-1}. At low annealing temperature (400 °C) the vibration of Si–OH bonds situated around 955 cm^{-1} and the shoulder at 1237-1233 cm^{-1} attributed to the stretching

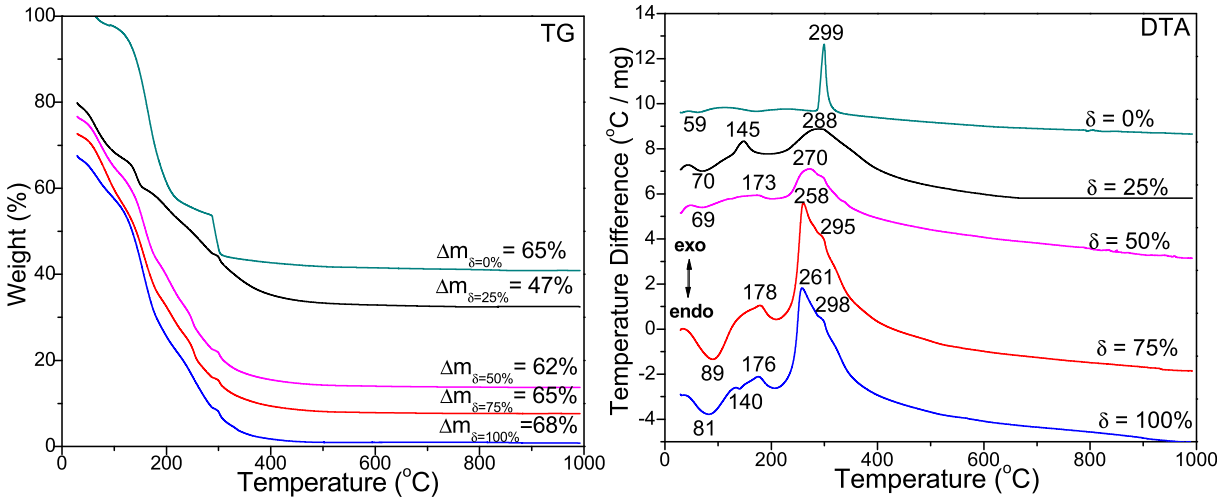

Fig. 1. TG and DTA diagrams of $(Zn_{0.5}Ni_{0.5}Fe_2O_4)_\delta$ $(SiO_2)_{100-\delta}$ samples heated at 40 °C.

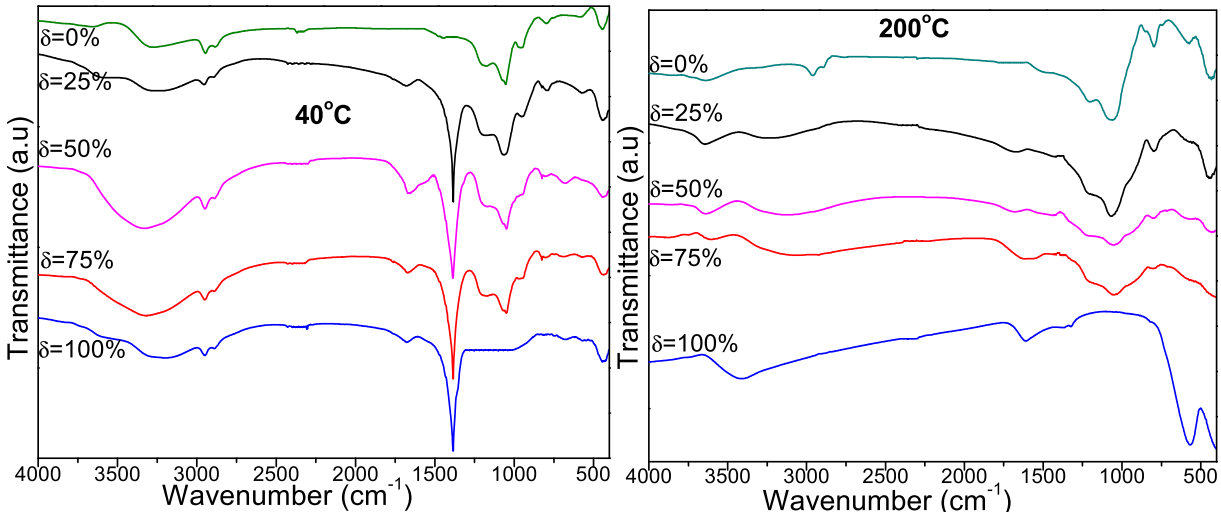

Fig. 2. FT-IR spectra of $(Zn_{0.5}Ni_{0.5}Fe_2O_4)_\delta$ $(SiO_2)_{100-\delta}$ samples heated at 40 and 200 °C.

vibration of Si–O–Si bonds, also appeared [15–18]. These bands are missing in the bulk $Zn_{0.5}Ni_{0.5}Fe_2O_4$ (δ = 100%) where only the presence of the bands around 580 cm^{-1} attributed to Zn–O and Ni–O vibration, and around 410 cm^{-1} attributed to Fe–O bonds vibration are observed [15–17].

3.3. Structural analysis

At all temperatures, for δ = 0%, the formation of the halo in the range 2θ = 16–28° corresponds to the amorphous SiO_2 (Fig. 3). A similar behavior was observed for the NCs with high SiO_2 matrix content (δ = 25%) annealed at 400 °C, while at 700 °C, the lines of $Ni_{0.5}Zn_{0.5}Fe_2O_4$ appear. The diffraction peaks of other crystalline phases are not evidenced, which confirms the formation of single-phase cubic spinel structure with space group *Fd3m* in agreement with JCPDS card no. 52–0278 [20]. The prominent (h k l) planes indexed by (111), (220), (311), (222), (400), (442), (511) and (440) are in excellent agreement with diffraction planes of $Ni_{0.5}Zn_{0.5}Fe_2O_4$ (Fig. 3). For NCs with high ferrite content (δ = 50 and 75%), the single-phase poorly crystalized $Zn_{0.5}Ni_{0.5}Fe_2O_4$ appears at 400 °C, the intensity of diffraction lines and degree of crystallinity reaching the maximum at 1000 °C. The intensity of diffraction lines increases at high annealing temperatures, due to the higher degree of crystallinity and low effects of inert surface layer of the crystals [12–14]. For bulk $Zn_{0.5}Ni_{0.5}Fe_2O_4$ (δ = 100%), the single-crystalline phase is already crystallized at 400 °C resulting in higher crystallite sizes compared to those of NCs with low ferrite content embedded in the SiO_2 matrix. There is no indication of any impurities or unreacted Fe-, Ni- and Zn-oxides, the broadening of diffraction peaks being attributed to ultrafine $Zn_{0.5}Ni_{0.5}Fe_2O_4$ particles present in the samples [12]. The (311) plane as the strongest reflection is indicative for the spinel phase [21]. Furthermore, the intensity of main diffraction peak of cubic spinel ferrite at (311) plane was considered as a measure of the degree of crystallinity [22]. The average crystallite sizes (D_{XRD}) were calculated from the full-width at half-maximum (FWHM) of diffraction peaks using the Debye Scherrer's equation (Table 1) [15–18]. The crystallite size increases with increasing annealing temperature and ferrite content embedded in the SiO_2 matrix. The variation of crystallite size may be due to peak broadening because of the lattice strains, thermal and instrumental effects [6]. Therefore, the highest value of crystallite size was obtained for bulk Ni–Zn ferrite, which may lead to

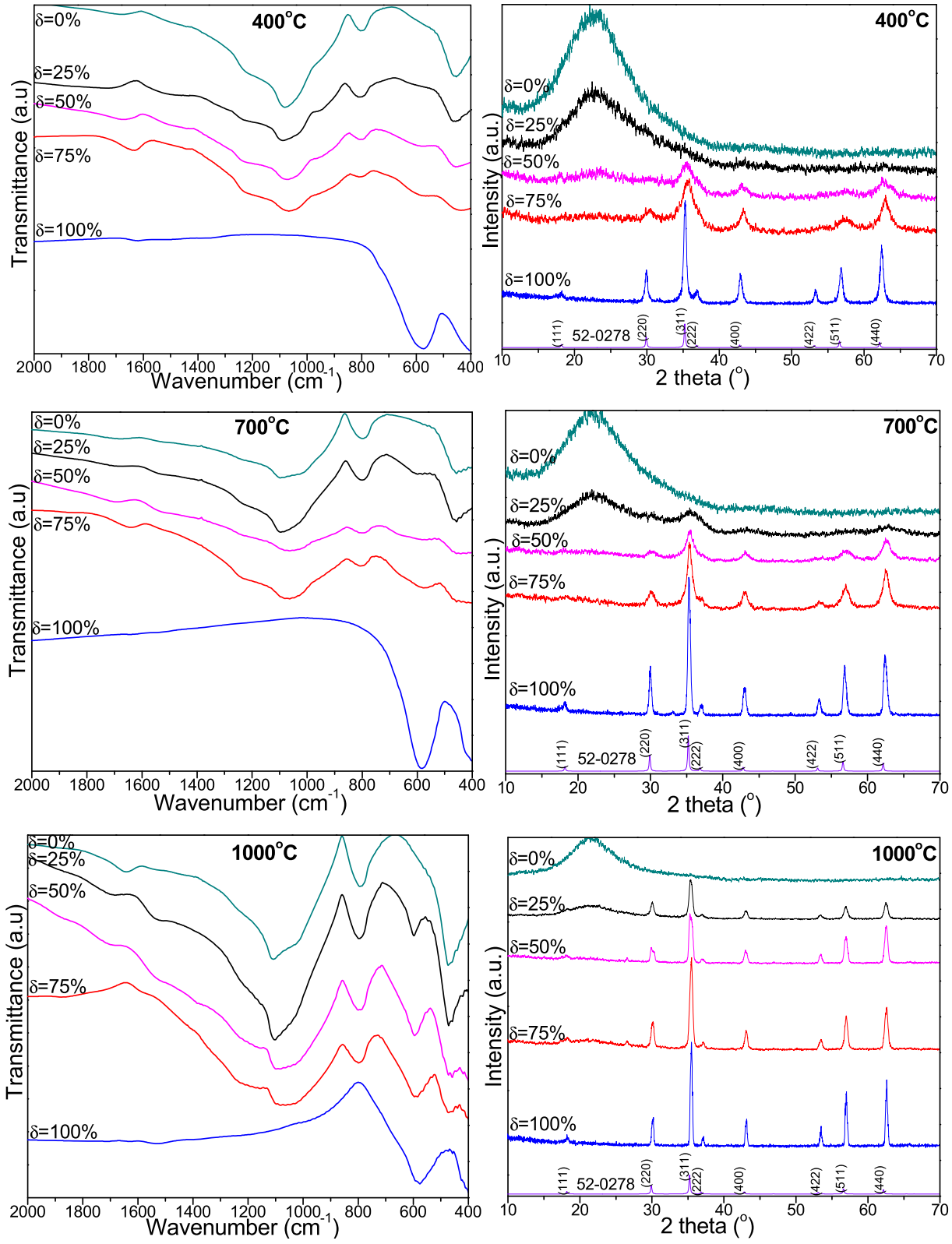

Fig. 3. FT-IR spectra and XRD patterns of $(Zn_{0.5}Ni_{0.5}Fe_2O_4)_\delta$ $(SiO_2)_{100-\delta}$ NCs annealed at 400, 700 and 1000 °C.

the assumption that the SiO_2 matrix contributes to crystallite size decrease. High SiO_2 content and low annealing temperature leads to highly amorphous content. However, it should be taken into account that not all the amorphous phases generate diffraction halos due to the lack of a significant local order. The area under the amorphous halo and the total area of the diffraction peaks corresponding to the crystalline phases were used to investigate the evolution of amorphous SiO_2 and crystalline $Zn_{0.5}Ni_{0.5}Fe_2O_4$

Table 1
Average crystallites size (D_{XRD}, nm), particle size (D_{TEM}, nm) and specific surface area (SSA, m^2/g) for $(Zn_{0.5}Ni_{0.5}Fe_2O_4)_\delta$ $(SiO_2)_{100-\delta}$ NCs annealed at 400, 700 and 1000 °C.

δ (%)	D_{XRD}			D_{TEM}			SSA		
	400 °C	700 °C	1000 °C	400 °C	700 °C	1000 °C	400 °C	700 °C	1000 °C
0	0	0	0	0	0	0	393	221	≤0.5
25	0	3.0	18.2	1	3	19	365	–	≤0.5
50	2.7	7.0	22.7	3	8	23	260	165	≤0.5
75	4.4	11.2	30.3	5	13	31	247	18	≤0.5
100	14.3	28.8	57.4	15	30	60	29	6	≤0.5

phases. At all annealing temperatures, it was considered 100% SiO_2 when only this phase was identified, when the amorphous halo is lacking.

The relative proportion of amorphous SiO_2 and crystalline $Zn_{0.5}Ni_{0.5}Fe_2O_4$ phases are presented in Fig. 4. For δ = 25–75%, the sum of crystalline and amorphous (SiO_2) phases is lower than 100%, leading to the assumption that there are still unidentified amorphous phases. The relative proportion of the amorphous (SiO_2) phase decreases (Fig. 4a), while the relative proportion of crystalline phases increases (Fig. 4b) with increasing annealing temperature. Thus, for δ = 0 and 25%, the content of the amorphous phase decreases markedly at high annealing temperatures. After reaching the equilibrium between the crystalline and amorphous phases (δ = 50%) a slower decrease of the amorphous and increase of crystalline phase is observed.

3.4. Surface analysis

The N_2 adsorption-desorption isotherms of $(Zn_{0.5}Ni_{0.5}Fe_2O_4)_\delta$ $(SiO_2)_{100-\delta}$ (δ = 0, 25, 50, 75, 100%) NCs annealed at 400 and 700 °C (Fig. 5) gives information about the porous structure of NCs. The shape of isotherms is preserved during the annealing at 400 and 700 °C, indicating that the porous structure is stable upon annealing up to 700 °C and collapse only at higher temperatures. The isotherms of the NCs annealed at 1000 °C were not recorded due to the collapse of the porous structure during annealing at high temperature.

As a result, the specific surface area (SSA) of these NCs was below the detection limit (0.5 m^2/g). All recorded isotherms are of type IV, typical for mesoporous materials [23]. For δ = 0, 25, 50 and 75% NCs a H4 type hysteresis loop on the desorption branch is observed. This type of hysteresis is usually associated with narrow slit-like pores. The H4 type hysteresis loop and the form of the isotherm at low pressures (similar with type I isotherm), indicate the presence of narrow pores situated in the low region of mesopores. This information is confirmed by the pore size distribution calculated with Dollimore Heal model, which show that for all materials which contain SiO_2 matrix (δ = 0, 25, 50 and 75%), the medium porosity is given by the matrix, all pores being lower than 6 nm. The H1 type hysteresis loop observed on the desorption branch of the isotherm for bulk $Zn_{0.5}Ni_{0.5}Fe_2O_4$ (δ = 100%) indicate the existence of agglomerates of spherical particles. The average specific pore volume ranges from 0.1829 to 0.022 cm^3/g at 400 °C and from 0.077 to 0.010 cm^3/g at 700 °C. The highest SSA calculated using BET model (Table 1) is obtained for SiO_2 matrix (δ = 0%) and the lowest for bulk $Zn_{0.5}Ni_{0.5}Fe_2O_4$ (δ = 100%) in accordance with the previous studies [24,25]. For NCs annealed at the same temperature, the SSA decreases with the increasing $Zn_{0.5}Ni_{0.5}Fe_2O_4$ content embedded in the SiO_2 matrix, due to the large difference between the total SSA of the matrix and of the ferrite. For the same NC, the SSA decreases with the increase of annealing temperature. The highest decrease of SSA with temperature is observed for δ = 75% NC, for which more than 90% of the SSA is lost by annealing at 700 °C compared to the NC annealed at 400 °C. A possible explanation could be the high content of Zn–Ni ferrite in this NC, which has low SSA and a much lower stability of porous structure at increased temperatures, compared to SiO_2 matrix.

3.5. TEM analysis

Fig. 6 shows the distribution, shape and size of $Zn_{0.5}Ni_{0.5}Fe_2O_4$ nanoparticles embedded in SiO_2 matrix for δ = 25–100% NCs annealed at 400, 700 and 1000 °C. The TEM images of SiO_2 matrix (δ = 0%) consist in a dark area, without any possibility to identify

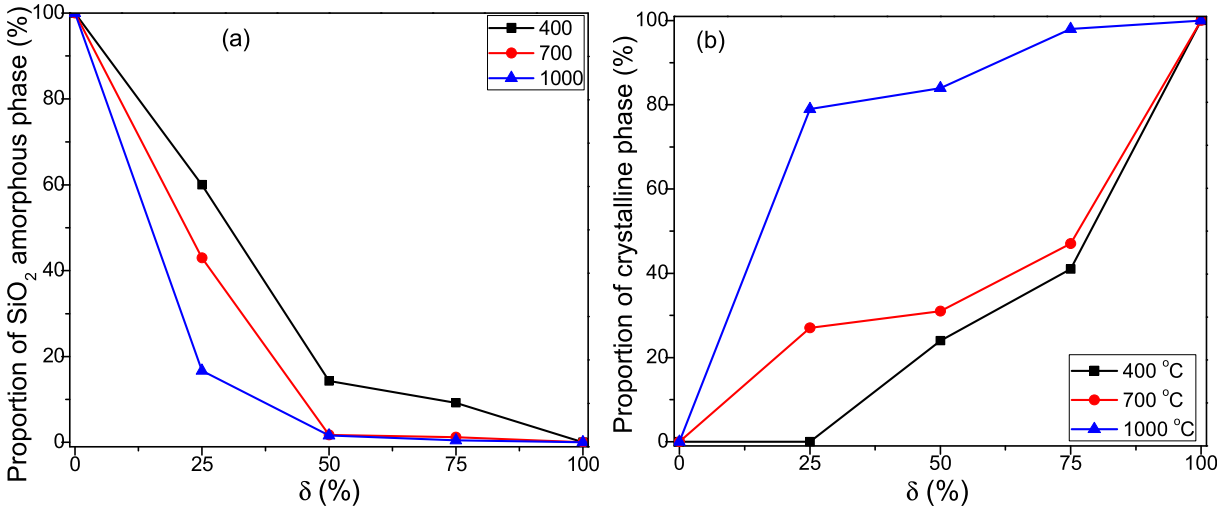

Fig. 4. Relative proportion of amorphous SiO_2 (a) and $Zn_{0.5}Ni_{0.5}Fe_2O_4$ crystalline phases (b) for $(Zn_{0.5}Ni_{0.5}Fe_2O_4)_\delta$ $(SiO_2)_{100-\delta}$ NCs.

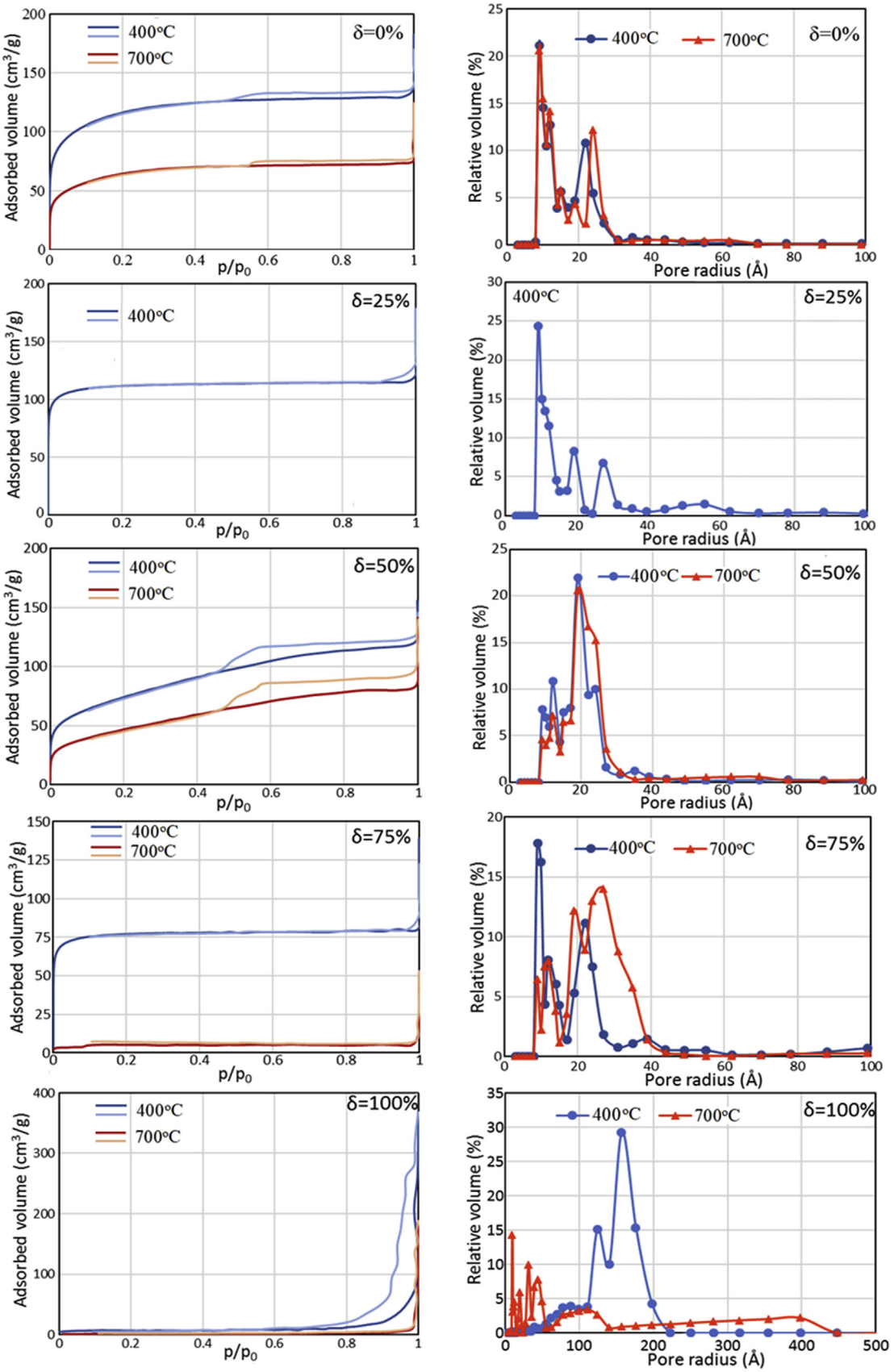

Fig. 5. N_2 adsorption-desorption isotherms and pore size distribution of $(Zn_{0.5}Ni_{0.5}Fe_2O_4)_\delta$ $(SiO_2)_{100-\delta}$ NCs annealed at 400 and 700 °C.

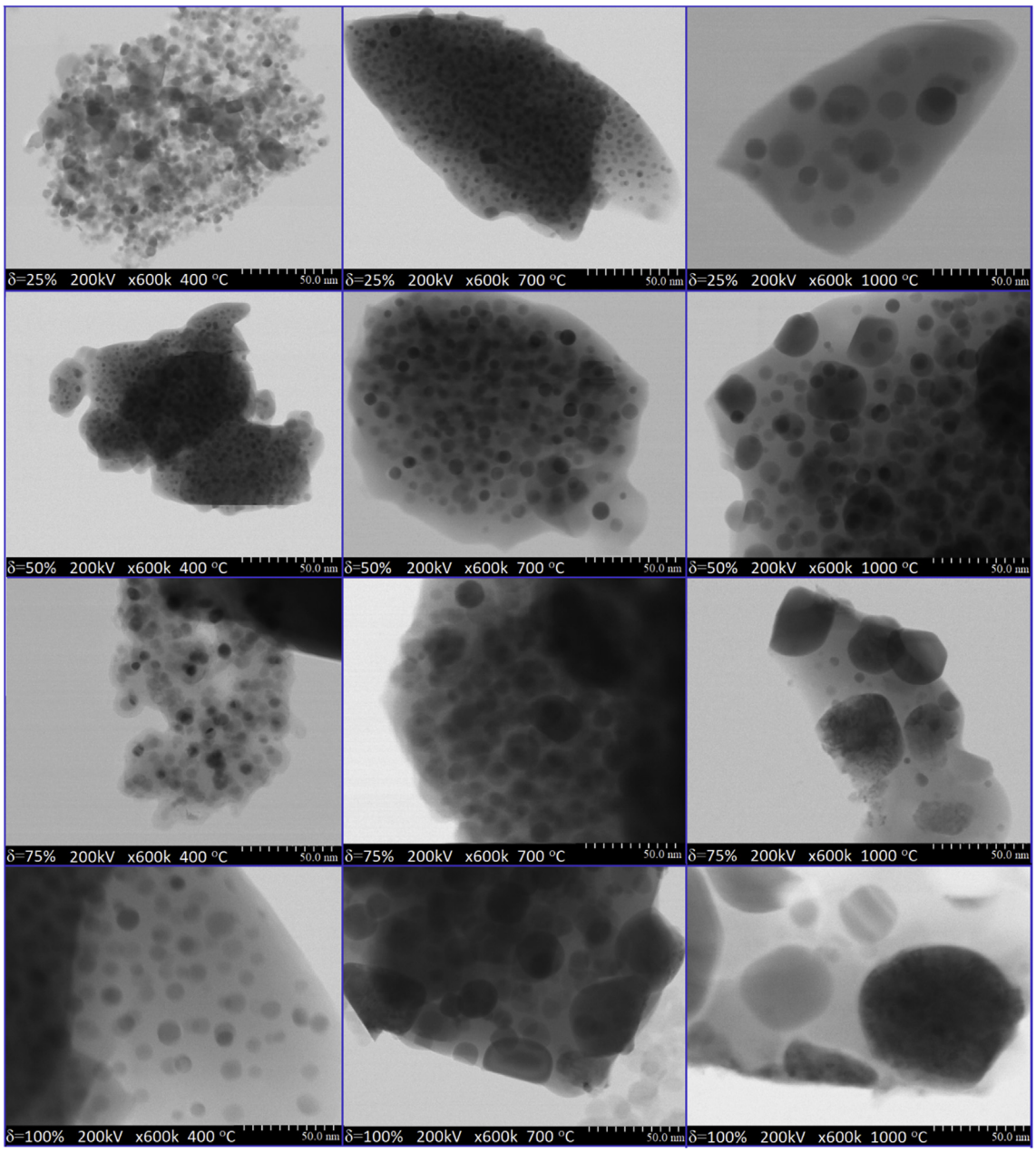

Fig. 6. TEM images of $(Zn_{0.5}Ni_{0.5}Fe_2O_4)_\delta$ $(SiO_2)_{100-\delta}$ NCs (δ = 25–100%) NCs annealed at 400, 700 and 1000 °C.

the matrix network. At 400 °C, the TEM images of δ = 25% NC are blurry, with low contrast due to the small sized insufficiently crystallized $Zn_{0.5}Ni_{0.5}Fe_2O_4$ particles (~1 nm). For δ = 50–100% NCs an increase of spherical particles diameter with the increase of ferrite content embedded in the SiO_2 matrix and the increase of annealing temperature is observed. The particle morphology and grain boundaries can affect the ferrites characteristics [26]. The particle size increases with the ferrite content from 1 to 15 nm (400 °C), 3–30 nm (700 °C) and 19–60 nm (1000 °C) (Fig. 6, Table 1). Oppositely to the other NCs, for bulk $Zn_{0.5}Ni_{0.5}Fe_2O_4$ (δ = 100%) much higher particle sizes are observed. For the same ferrite content, the particles size increases with the increase of the annealing temperature, due to the formation of crystalline clusters as a result of the higher crystal growth rate, following the volume expansion and reduction of system supersaturation, at high temperatures. This behavior suggests that the nanocrystallite size is influenced by the annealing temperature [15–17]. When the nucleation rate is higher than the growth rate, small and homogenously distributed particles are obtained, while at the high annealing temperatures, the particle size increases due to coalescence [16].

Crystallite sizes estimated from XRD are consistent with the particle sizes evaluated from TEM. The low differences between the results obtained by XRD and TEM could be explained by the interference of amorphous SiO_2 and large-size nanoparticles that give important contribution to the diffraction patterns, as they contain a large fraction of the total number of atoms [16].

3.6. VSM properties

Fig. 7 shows the magnetic hysteresis loops, the saturation magnetization (M_S), remanent magnetization (M_R) and coercive

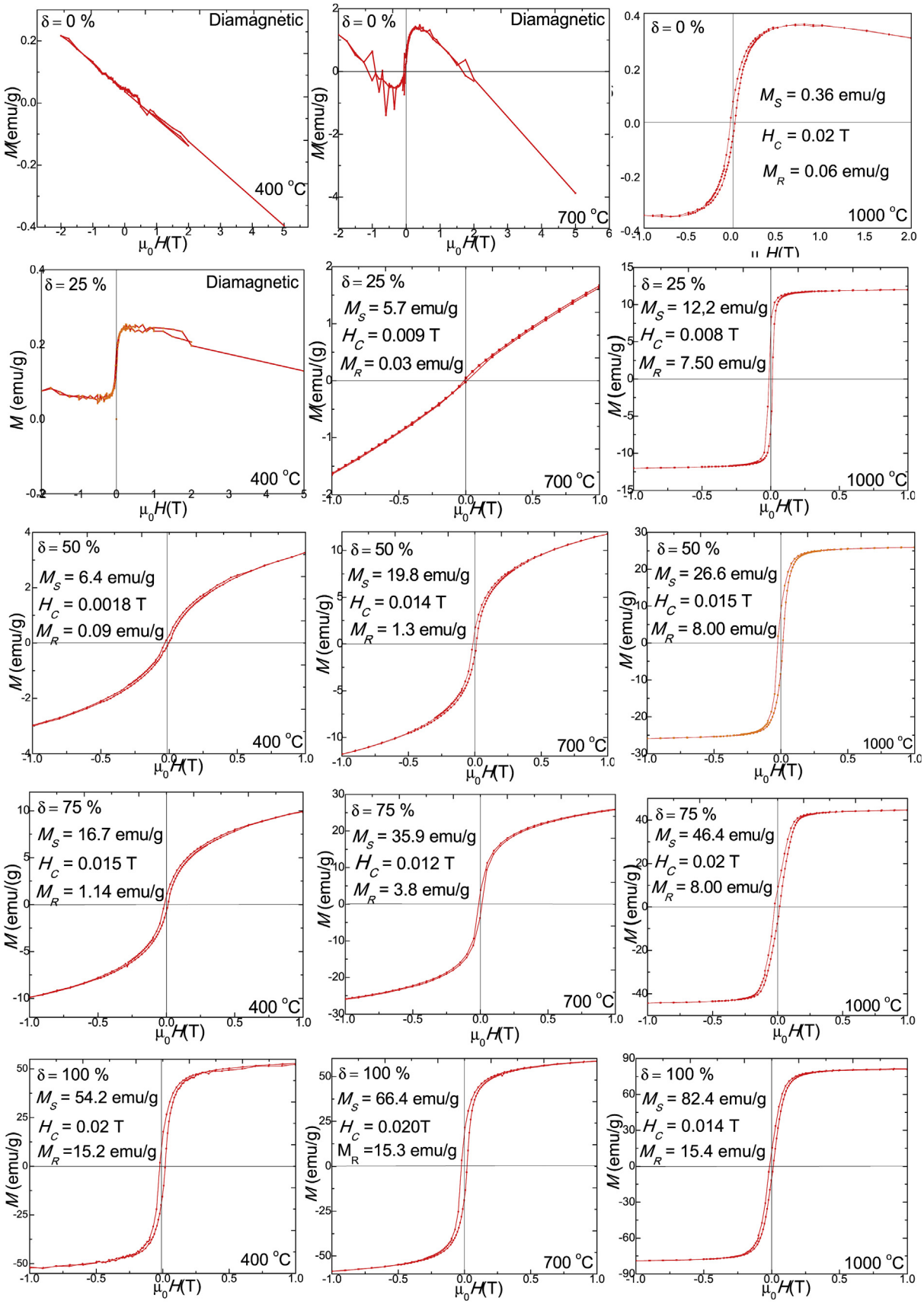

Fig. 7. Magnetic hysteresis loop of $(Zn_{0.5}Ni_{0.5}Fe_2O_4)_\delta$ $(SiO_2)_{100-\delta}$ NCs (δ = 0–100%) annealed at 400, 700 and 1000 °C.

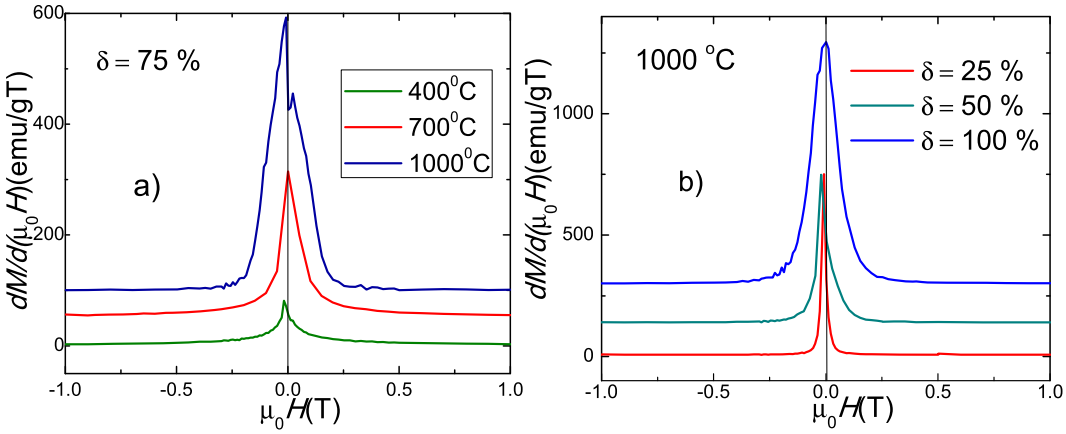

Fig. 8. Magnetization derivative of $(Zn_{0.5}Ni_{0.5}Fe_2O_4)_\delta$ $(SiO_2)_{100-\delta}$ NCs (δ = 75%) annealed at 400, 700 and 1000 °C (a) and $(Zn_{0.5}Ni_{0.5}Fe_2O_4)_\delta$ $(SiO_2)_{100-\delta}$ NCs (δ = 25, 50 and 100%) annealed at 1000 °C (b).

field (H_C) values, while Fig. 8 shows the magnetization derivatives ($dM/d(\mu_0 H)$) of $(Zn_{0.5}Ni_{0.5}Fe_2O_4)_\delta$ $(SiO_2)_{100-\delta}$ (δ = 0, 25, 50, 75, 100) NCs annealed at 400, 700 and 1000 °C. The SiO_2 matrix (δ = 0%) annealed at 400 °C has a diamagnetic behavior, while after annealing at higher temperatures (700 and 1000 °C) shows a diamagnetic behavior at high magnetic fields and ferromagnetic behavior in the region of low magnetic fields. A similar behavior exhibits the sample with δ = 25% annealed at 400 °C. The fraction of the ferromagnetic phase in the δ = 25% NC increases with increasing annealing temperature, and the ferromagnetic behavior became dominant when the annealing temperature is higher than 400 °C. For δ = 50–75% NCs, a significant increase of M_S and M_R appears with increasing annealing temperature, resulting in a superparamagnetic behavior. For the bulk $Zn_{0.5}Ni_{0.5}Fe_2O_4$ (δ = 100%), the M_S substantially increases, in comparison with the ferrites embedded in SiO_2 matrix (δ = 25–75%), at all annealing temperatures, while the M_R is nearly constant for the NCs annealed at 400, 700 and 1000 °C, presenting a ferromagnetic behavior. The superparamagnetic behavior of these nanoparticles results from their extremely low crystallite sizes which have low anisotropy energy allowing an easy thermal activation [14]. In the case of bulk $Zn_{0.5}Ni_{0.5}Fe_2O_4$ (δ = 100%), for all annealing temperatures, typical hysteresis loops for room temperature ferromagnetism were obtained. This behavior is a consequence of the larger crystallite sizes, as found from XRD and TEM investigations. Generally, the increase of annealing temperature improves the magnetic parameters (M_S and M_R) of the NCs, due to enhancement of the $Zn_{0.5}Ni_{0.5}Fe_2O_4$ crystallinity, increase of interatomic distances, occurrence of vacancies, reduction of the coordination number.

The M_S values obtained in this study are rather different from the previously reported data [1,3,6,7,12,26]. The low M_S values of NCs annealed at low temperatures could be explained by the low crystallinity degree, occurrence of vacancies, interatomic spacing and low coordination number. They are also the consequence of lattice defects which results in a weak magnetic super-exchange interaction between A and B sites [16,17]. Another contribution to the M_S comes from the spin disorder on the surface of the nanoparticles [14]. The magnetization process occurs by domain wall motion and by magnetic moment rotation. The former requires less energy than the latter [7]. When Zn is introduced in the ferrite, the sizes of the grains grow and as a consequence the number of magnetic domains increases and the role of the wall movement become more important than that of the domain rotation [7]. When the grain sizes are at nanoscale, the surface energy highly increases and it can change the typical occupancy of the cation's sites [26]. The variation of the surface energy results mainly from the difference between the exchange energy of the ions from the surface and of the ions from the cores of the particles [26]. The change of cation occupancy increases the number of anti-site defects which will determine the change of magnetization [26]. In large size grains, a large number of magnetic domain walls will form and the domain wall motion will become dominant over the domain rotation contribution to magnetization. This process is also enhanced by the decrease of the magnetocrystalline anisotropy [1].

The H_C has relatively low values ranging between 0.009 and 0.02 T, the largest value belonging to bulk $Zn_{0.5}Ni_{0.5}Fe_2O_4$ (δ = 100%). The sharp peak curves of magnetization derivative (dM/d(μ0H)) vs. applied magnetic field (Fig. 8) are typical for high magnetic purity phases, while the broad peaks indicate a wide distribution of particle sizes. For δ = 25–100% NCs, these curves show sharp peaks suggesting the presence of a magnetic pure phase; however, some depreciation in the purity of the magnetic phase is observed for the NCs annealed at 400 °C.

Several nano-crystalline oxides such as CeO_2, Al_2O_3, ZnO, In_2O_3, SnO_2 [27], MgO [28] were found to have magnetic properties, while they have diamagnetic behavior in bulk samples. Usually, the measured M_S of these oxides is quite small, around 10^{-3} emu/g, but in the case of 170 nm thin MgO films, the M_S reaches 1.58 emu/g [28]. Such a behavior was presumed to have its origin in the exchange interactions between localized electron spin moments resulting from the oxygen vacancies on the nanoparticle surfaces [27,28]. This scenario could be valid also for our nano-sized SiO_2 matrix, if we assume that the defects in the form of vacancies are the source of the ferromagnetic behavior. However, the magnetization (0.36 emu/g) of the δ = 0% NC annealed at 1000 °C is rather high to be caused only by this exchange interactions. Another scenario could be the accidental contamination of the nanopowders during handling [29]. As it can be seen, at high magnetic fields the diamagnetic behavior began to be dominant for these samples. The epoxy resin contribution to M_S of our NCs is marginal since it has a diamagnetic susceptibility of −0.009 emu/(g·T). For the bulk ferrite the saturation magnetization has high values (54.2–82.4 emu/g for the NCs annealed at 400 and 1000 °C respectively) making the magnetic contribution of the SiO_2 matrix to be insignificant. Thus, we could say that the SiO_2 coating of the nanoparticles, enhances the surface spin disorder effects, resulting in a lower fraction of active magnetic atoms, that further leads to the reduction of the saturation magnetization.

4. Conclusions

In this paper, $\delta Zn_{0.5}Ni_{0.5}Fe_2O_4/(100\text{-}\delta)SiO_2$ NCs with $\delta = 0$, 25, 50, 75 and 100% were prepared by sol-gel method, followed by annealing at 400, 700 and 1000 °C. According to XRD, amorphous SiO_2 matrix in case of $\delta = 0\%$ and cubic spinel $Zn_{0.5}Ni_{0.5}Fe_2O_4$ in case of $\delta = 25–100\%$ were obtained. In all cases, the proportion of the crystalline $Zn_{0.5}Ni_{0.5}Fe_2O_4$ phase increases, with increasing annealing temperature. For NCs ($\delta = 25–75\%$), the crystallite size of $Zn_{0.5}Ni_{0.5}Fe_2O_4$ increases with increasing ferrite content embedded in the SiO_2 matrix. The bulk $Zn_{0.5}Ni_{0.5}Fe_2O_4$ ($\delta = 100\%$) starts to crystallize around 400 °C and have larger particle size than the ferrites embedded in SiO_2 matrix. In each case, the crystallite size significantly increases with increasing annealing temperature. The SSA (from 393 to 29 m^2/g at 400 °C and from 221 to 6 m^2/g at 700 °C) and specific pore volume (from 0.183 to 0.010 cm^3/g) decreases with increasing ferrite content and annealing temperature (at 1000 °C being lower than 0.5 m^2/g). The H_C has low values, ranging between 0.009 and 0.02 T. The M_S and M_R improve with increasing ferrite content embedded in SiO_2 and with increasing annealing temperature. For the bulk $Zn_{0.5}Ni_{0.5}Fe_2O_4$, the M_R stabilizes around 15.3 emu/g. As expected, bulk $Zn_{0.5}Ni_{0.5}Fe_2O_4$ ($\delta = 100\%$) is ferromagnetic, the SiO_2 matrix ($\delta = 0\%$) is diamagnetic with a small ferromagnetic fraction, while the $Zn_{0.5}Ni_{0.5}Fe_2O_4$ embedded in SiO_2 is superparamagnetic.

Declaration of competing interest

The authors declare that they have no known competing financial interests or personal relationships that could have appeared to influence the work reported in this paper.

CRediT authorship contribution statement

Thomas Dippong: Formal analysis, Writing - original draft. **Oana Cadar:** Formal analysis, Writing - original draft. **Iosif Grigore Deac:** Formal analysis, Writing - original draft. **Mihaela Lazar:** Formal analysis, Writing - original draft. **Gheorghe Borodi:** Formal analysis, Writing - original draft. **Erika Andrea Levei:** Formal analysis, Writing - original draft.

Acknowledgements

This work was supported by the Romanian Ministry of Research and Innovation through Institutional Performance-Projects for Financing Excellence in RDI [grant number 19PFE/2018 and 32PFE/2018], Researcher Mobility [grant number 117MC/2019], Complex Projects of Frontier Research [grant number 6/2018] and NUCLEU Program [grant number PN 19 35 02 02]. The authors would like to express their gratitude to Dr. Razvan Hirian and Marc du Plessis for the magnetic measurements and to Dr. Lucian Barbu-Tudoran for the TEM measurements.

References

[1] S. Atiq, M. Majeed, A. Ahmada, S.K. Abbas, M. Saleem, S. Riaz, S. Nassem, Synthesis and investigation of structural, morphological, magnetic, dielectric and impedance spectroscopic characteristics of Ni-Zn ferrite nanoparticles, Ceram. Int. 43 (2017) 2486–2494, https://doi.org/10.1016/j.ceramint.2016.11.046.

[2] A. Hajalilou, S.A. Mazlan, K. Shameli, A comparative study of different concentrations of pure Zn powder effects on synthesis, structure, magnetic and microwave-absorbing properties in mechanically-alloyed Ni-Zn ferrite, J. Phys. Chem. Solid. 96–97 (2016) 49–59, https://doi.org/10.1016/j.jpcs.2016.05.001.

[3] A.A. El-Fadi, A.M. Hassan, M.H. Mahmoud, T. Tatarchuk, I.P. Yaremiy, A.M. Gismelssed, M.A. Ahmed, Synthesis and magnetic properties of spinel $Zn_{1-x}Ni_xFe_2O_4$ ($0 \leq x \geq 1.0$) nanoparticles synthesized by microwave combustion method, J. Magn. Magn Mater. 471 (2019) 192–199, https://doi.org/10.1016/j.jmmm.2018.09.074.

[4] A. Safari, K. Gheisari, M. Farbod, Structural, microstructural, magnetic and dielectric properties of Ni-Zn ferrite powders synthesized by plasma arc discharge process followed by post-annealing, J. Magn. Magn Mater. 488 (2019), 165369, https://doi.org/10.1016/j.jmmm.2019.165369.

[5] M. Gharagozlou, Study on the influence of annealing temperature and ferrite content on the structural and magnetic properties of $x(NiFe_2O_4)/(100\text{-}x)SiO_2$, J. Alloys Compd. 495 (2010) 217–223, https://doi.org/10.1016/j.jallcom.2010.01.128.

[6] M.K. Anupama, B. Rudraswamy, N. Dhananjaya, Investigation on impedance response and dielectric relaxation of Ni-Zn ferrites prepared by self-combustion technique, J. Alloys Compd. 706 (2017) 554–561, https://doi.org/10.1016/j.jallcom.2017.02.241.

[7] A.S. Džunuzović, N.I. Ilić, M.M. Vijatović Petrović, J.D. Bobić, B. Stojadinović, Z. Dohčević-Mitrović, B.D. Stojanović, Structure and properties of Ni-Zn ferrite obtained by auto-combustion method, J. Magn. Magn Mater. 374 (2015) 245–251, https://doi.org/10.1016/j.jmmm.2014.08.047.

[8] C.A.P. Gomez, C.A.B. Meneses, A. Matute, Structural parameters and cation distributions in solid state synthesized Ni-Zn ferrite, Mater. Sci. Eng. B 236–237 (2018) 48–55, https://doi.org/10.1016/jmseb.2018.12.003.

[9] Y. Wang, X. Gao, X. Wu, W. Zhang, C. Luo, P. Liu, Facile design of 3D hierarchical $NiFe_2O_4$/N-CN/ZnO composites as a high-performance electromagnetic wave absorber, Chem. Eng. J. 375 (2019), 121942, https://doi.org/10.1016/j.cej.2019.121942.

[10] Y. Wang, Y. Fu, X. Wu, W. Zhang, Q. Wang, J. Li, Synthesis of hierarchical core-shell $NiFe_2O_4$ @MnO_2 composite microsphere decorated graphene nanosheet for enhanced microwave absorption performance, Ceram. Int. 43 (14) (2017) 11367–11375, https://doi.org/10.1016/j.ceramint.2017.05.344.

[11] Y. Wang, X. Gao, L. Zhang, X. Wu, Q. Wang, C. Luo, G. Wu, Synthesis of Ti3C2/Fe3O4/PANI hierarchical architecture composite as an efficient wide-band electromagnetic absorber, Appl. Surf. Sci. 480 (2019) 830–838, https://doi.org/10.1016/j.apsusc.2019.03.049.

[12] C. Srinivas, B.V. Tirupanyam, S.S. Meena, S.M. Yusuf, C. Seshu Babu, K.S. Ramakrishma, D.M. Potukuchi, D.L. Sastry, Structural and magnetic characterization of co-precipitated $Ni_xZn_{1-x}Fe_2O_4$ ferrite nanoparticles, J. Magn. Magn Mater. 407 (2016) 135–141, https://doi.org/10.1016/j.jmmm.2016.01.060.

[13] D. Guo, C. Jiang, X. Fan, H. Shi, D. Xue, Post-deposition heat-treated $Ni_xZn_{1-x}Fe_2O_4$ films exhibiting higher resonance frequency, Appl. Surf. Sci. 258 (2012) 4237–4239, https://doi.org/10.1016/j.apsusc.2011.12.058.

[14] A. Kumar, A. Singh, M.S. Yadav, M. Arora, R.P. Pant, Finite size effect on Ni doped nanocrystalline $Ni_{1-x}Zn_xFe_2O_4$ ($0.1 \leq x \geq 0.5$), Thin Solid Films 519 (2010) 1056–1058, https://doi.org/10.1016/j.tsf.2010.08.043.

[15] T. Dippong, E.A. Levei, C. Tanaselia, M. Gabor, M. Nasui, L. Barbu Tudoran, G. Borodi, Magnetic properties evolution of the $Co_xFe_{3-x}O_4/SiO_2$ system due to advanced thermal at 700 °C and 1000 °C, J. Magn. Magn Mater. 410 (2016) 47–54, https://doi.org/10.1016/j.jmmm.2016.03.020.

[16] T. Dippong, E.A. Levei, O. Cadar, I.G. Deac, L. Diamandescu, L. Barbu Tudoran, Effect of nickel content on structural, morphological and magnetic properties of $Ni_xCo_{1-x}Fe_2O_4/SiO_2$ nanocomposites, J. Alloys Compd. 786 (2019) 330–340, https://doi.org/10.1016/j.jallcom.2019.01.363.

[17] T. Dippong, I.G. Deac, O. Cadar, E.A. Levei, L. Diamandescu, G. Borodi, Effect of Zn content on structural, morphological and magnetic behavior of $Zn_xCo_{1-x}Fe_2O_4/SiO_2$ nanocomposites, J. Alloys Compd. 792 (2019) 432–443, https://doi.org/10.1016/j.jallcom.2019.04.059.

[18] T. Dippong, E.A. Levei, O. Cadar, Preparation of $CoFe_2O_4/SiO_2$ nanocomposites at low temperatures using short chain diols, J. Chem. (2017), 7943164, https://doi.org/10.1155/2017/7943164.

[19] L.K. Chuan, H.M. Zaid, Zinc composition and its effect on magnetic properties of nickel-zinc ferrite prepared via sol-gel technique, Am. J. Appl. Sci. 15 (2018) 121–123, https://doi.org/10.3844/ajassp.2018.121.123.

[20] Joint Committee on Powder Diffraction Standards, -International Center for Diffraction Data, 1999.

[21] H. Ghayour, M. Abdellahi, N. Ozada, S. Jabbrzare, A. Khandan, Hyperthermia application of zinc doped nickel ferrite nanoparticles, J. Phys. Chem. Solids 111 (2017) 464–472, https://doi.org/10.1016/j.jpcs.2017.08.018.

[22] G. Padmapriya, A. Manikandan, V. Krishnasamy, S.K. Jaganathan, S. Arul Antony, Spinel $Ni_xZn_{1-x}Fe_2O_4$ ($0.0 \leq x \geq 1.0$) nano-photocatalysts: synthesis, characterization and photocatalytic degradation of methylene blue dye, J. Mol. Struct. 1119 (2016) 39–47, https://doi.org/10.1016/j.molstruc.2016.04.049.

[23] K.S.W. Sing, D.H. Everett, R.A.W. Haul, L. Moscou, R.A. Pierotti, J. Rouquerol, T. Siemieniewska, Physical and biophysical chemistry division commission on colloid and surface chemistry including catalysis, Pure Appl. Chem. 57 (1985) 603–619, https://doi.org/10.1351/pac198557040603.

[24] Z. Liu, J. Zhu, C. Peng, T. Wakihara, T. Okubo, Continuous flow synthesis of ordered porous materials: from zeolites to metal-organic frameworks and mesoporous silica, React. Chem. Eng. 4 (2019) 1699–1720, https://doi.org/10.1039/C9RE00142E.

[25] A. Pathania, P. Thakur, A.V. Trukhanov, S.V. Trukhanov, L.V. Panina, U. Luders, A. Thakur, Development of tungsten doped Ni-Zn nano-ferrites with fast response and recovery time for hydrogen gas sensing application, Results Phys. 15 (2019) 10253, https://doi.org/10.1016/j.rinp.2019.102531.

[26] H. Bakhshi, N. Vahdati, A. Sedghi, Y. Mozharivskyj, Comparison of the effect of nickel and cobalt cations addition on structural and magnetic properties of

manganese-zinc ferrite nanoparticles, J. Magn. Magn Mater. 474 (2019) 56–62, https://doi.org/10.1016/j.jmmm.2018.10.146.
[27] A. Sunderasen, R. Bhavari, N. Rangarajan, U. Siddesh, C.N.R. Rao, Ferromagnetism as a universal feature of nanoparticles of the otherwise nonmagnetic oxides, Phys. Rev. B 74 (R) (2006), 161306, https://doi.org/10.1103/PhysRevB.74.161306.
[28] M. Kapilashrami, J. Xu, K.V. Rao, L. Belova, E. Carlegrim, M. Fahlman, Experimental evidence for ferromagnetism at room temperature in MgO thin films, J. Phys. Condens. Matter 22 (2010), 3450004, https://doi.org/10.1088/0953-8984/22/34/345004.
[29] M.A. Garcia, E. Fernandez, Pinel, J. de la Venta, A. Quesada, V. Bouzas, J.F. Fernández, J.J. Romero, M.S. Martín González, J.L. Costa-Krämer, Sources of experimental errors in the observation of nanoscale magnetism, J. Appl. Phys. 105 (2009), 013925, https://doi.org/10.1063/1.3060808.